Appl. Phys. B 75, 281–288 (2002)
DOI: 10.1007/s00340-002-0948-y

Applied Physics B
Lasers and Optics

D. RICHTER[1,✉]
A. FRIED[1]
B.P. WERT[1]
J.G. WALEGA[1]
F.K. TITTEL[2]

Development of a tunable mid-IR difference frequency laser source for highly sensitive airborne trace gas detection

[1] National Center for Atmospheric Research, 1850 Table Mesa Dr., Boulder, CO 80305, USA
[2] Rice Quantum Institute, Rice University, 6100 Main St. Houston, TX 77005, USA

Received: 29 April 2002
Published online: 21 August 2002 •

ABSTRACT The development of a compact tunable mid-IR laser system at 3.5 μm for quantitative airborne spectroscopic trace gas absorption measurements is reported. The mid-IR laser system is based on difference frequency generation (DFG) in periodically poled $LiNbO_3$ and utilizes optical fiber amplified near-IR diode and fiber lasers as pump sources operating at 1083 nm and 1562 nm, respectively. This paper describes the optical sensor architecture, performance characteristics of individual pump lasers and DFG, as well as its application to wavelength modulation spectroscopy employing an astigmatic Herriott multipass gas absorption cell. This compact system permits detection of formaldehyde with a minimal detectable concentration (1σ replicate precision) of 74 parts-per-trillion by volume (pptv) for 1 min of averaging time and was achieved using calibrated gas standards, zero air background and rapid dual-beam subtraction. This corresponds to a pathlength-normalized replicate fractional absorption sensitivity of 2.5×10^{-10} cm^{-1}.

PACS 42.55.Wd; 42.60.By; 42.60.Jf; 42.62.Fi; 42.79.Nv

1 Introduction

Sensitive and selective measurements of various trace atmospheric constituents have been carried out employing mid-infrared (mid-IR) laser absorption spectroscopy to access strong and well-resolved fundamental ro-vibrational absorption features. One can cite numerous examples where cryogenically cooled lead-salt diode lasers have traditionally been used for this purpose and the reader is referred to Werle [1] and references therein. Other semiconductor laser sources based on Sb III-V diode lasers, sources based on difference frequency generation (DFG) and distributed feedback (DFB) quantum cascade have been developed in recent years and employed for atmospheric studies [2]. Other solid-state laser sources based on Cr-doped solid-state and line-tunable CO and CO_2 gas lasers have also been employed for this purpose [3, 4]. In addition, a variety of spectroscopic signal enhancing and noise reduction techniques have been developed [5]. Each laser source combined with a signal enhancing technique provides unique advantages as well as limitations. For atmospheric studies, one frequently carries out trace gas measurements on airborne platforms where a variety of adverse physical operating conditions are often present. Such an environment requires that the overall laser spectroscopic system must be immune to severe vibrations, shock, acceleration and large changes in the operating temperature and pressure. These perturbations may ultimately limit the performance of a highly sensitive laboratory-based spectroscopic system, thus obviating its usefulness in field applications.

Spectroscopic gas detection systems based upon cryogenically cooled lead-salt diode lasers have been successfully operated in a host of rugged field environments, including airborne platforms. By careful attention to detail, such systems have been able to achieve very high sensitivity. For example, airborne measurements of formaldehyde (CH_2O) by Fried et al. performed during the TOPSE [6] 2000 campaign demonstrated absorption sensitivities ($A_{\min}$) of $1-2 \times 10^{-6}(1\sigma)$ for 1 min of averaging [7], using a pathlength of 100 m, a sampling pressure of 5.3 kPa and a sampling temperature of 30 °C. This corresponds to a CH_2O mixing ratio of 30 to 60 parts-per-trillion by volume (pptv, 1 pptv $= 1 \times 10^{-12}$). This performance assessment was determined from the replication precision associated with sampling constant ambient CH_2O levels, particularly very low ambient levels where the retrieved signals are close to those from the baseline. The replication precision along with instrument accuracy and response time are the most important figures of merit for atmospheric studies, and throughout the remainder of this paper we will employ these figures of merit. While the current airborne Pb-salt CH_2O performance is sufficient for some atmospheric studies, even higher sensitivities are required for studies of the background atmosphere where CH_2O mixing ratios approach levels as low as 20–30 pptv. In this case, it would be desirable to achieve sensitivities around 5–10 pptv ($A_{\min} = 1.7 \times 10^{-7}$). The performance of our present airborne system is not limited by residual amplitude modulation (RAM) noise [8], but rather by small changes in the spectral background structure due to subtle alignment changes, particularly when the aircraft changes attitude and/or cabin pressure. While small performance enhancements may be realized with additional mechanical improvements, and a factor of 2 improvement in detectable CH_2O concentration is possible using a 210 m multi-pass absorption cell, it would be highly desirable to achieve the requisite factor of ~ 6 improvement with a more compact system. DFG-based laser

✉ Fax: +1-303/497-1492, E-mail: dr@ucar.edu

sources (described and evaluated in this paper) possess numerous advantages over lead-salt diode lasers and thus it may be possible to achieve the aforementioned requisite enhancements employing such a laser [9]. The present paper, which builds upon the experiences of previous DFG source developments, describes a more systematic and longer-term effort to develop and employ a DFG laser source as a replacement for a Pb-salt diode laser capable of a higher CH_2O detection sensitivity than is presently available. As will be discussed, the new DFG-based laser source has far superior output beam quality than the Pb-salt diode laser. This output beam can be injected into multi-pass absorption cells with only one optical focusing element. Both aspects are important for optimizing the beam pointing stability and ultimately the instrument performance.

2 Difference frequency generation (DFG)-based mid-IR source

A number of optical designs for difference frequency generation (DFG) have been reported using a variety of visible and near-IR low- and high-power laser sources, discrete and fiber optics and non-linear frequency conversion optical materials [10–14]. The use of optical telecommunication lasers and key optical fiber elements offer significant improvements over past designs in many regards and provide unique advantages over direct mid-IR sources such as lead-salt and quantum cascade laser sources. The architecture of the modular mid-IR tunable source developed in this study is depicted in Fig. 1. Such a DFG-based source is divided into three all-optical-fiber-coupled modules, namely low-power seed laser sources operating at the 1 and 1.5 μm wavelength regions, high-power optical fiber amplifiers (OFA) and a mid-IR frequency conversion module. Unlike most other continuous wave (cw) mid-IR (2–5 μm) semiconductor lasers, the cw DFG-based source presented here operates at room temperature, offers inherent sub-MHz linewidths and mW-level optical output power without the need of an active feedback loop or frequency references. This provides optimal selectivity and absorption signal strength of a given absorption line at typical gas sampling pressures of ∼ 6 kPa. Due to similar temperature tuning coefficients of both seed laser sources of $\sim 0.3\,\mathrm{cm^{-1}K^{-1}}$, external temperature changes are effectively canceled, thus providing an inherent passive frequency stabilization of better than $25\,\mathrm{MHz\,h^{-1}}$ (peak-to-peak) [15]. The seed laser signals of 6 mW and 15 mW for the fiber and diode laser, respectively, are amplified to the Watt level by rare-earth-doped Yb and Er optical fibers. OFAs can be treated as passive components which amplify the signals and retain all other spectroscopic characteristics of the input laser signal, such as linewidth. In addition, OFAs provide gain over a spectral bandwidth of as large as 100 nm in the near-IR. Thus, for a given system, different seed wavelengths spanning the gain bandwidth region of the rare-earth optical fiber can be coupled using wavelength division multiplexers (WDM), and can be amplified, either at the same time or sequentially. After passing through the OFAs, the two seed wavelengths are combined by a low insertion loss WDM (0.05 dB at 1562 nm; 0.13 dB at 1083 nm). Both beams are now propagating in the same single spatial mode optical fiber. Typical mode-field diameters are 6 μm and 9 μm for wavelengths of 1 μm and 1.5 μm, respectively. Both beams are imaged ($M \sim 11$) from the single mode fiber tip (FC-APC) into a 50-mm-long, 11-mm-wide and 1-mm thick periodically poled $LiNbO_3$ crystal (PPLN) using a $f = 10$ mm near-IR achromatic microscope objective. The PPLN crystal is temperature-stabilized at 40 °C and incorporates eight different 'channels' of ∼ 1.3 mm width, with grating periods ranging from 29.7 to 30.5 μm in increments of 0.1 μm. For first order quasi phase-matching (QPM) of the pump wavelengths (1083 nm and 1562 nm) and the DFG wavelength (3.53 μm), the optical axis is aligned with the center channel with a nominal grating period of $\Lambda = 30.1$ μm. The PPLN crystal can be translated perpendicular to the optical axis in order to access a channel for a given input wavelength pair (i.e. 1030–1100 nm and 1530 nm–1570 nm) to quasi phase-match and generate coherent tunable mid-IR radiation between 3 μm and 3.9 μm. As depicted in Fig. 1, all laser beams propagate in optical fibers up to the DFG frequency conversion module. To configure the DFG source for a new mid-IR wavelength, appropriate seed sources are replaced or added by fusion-spliced optical connections. In turn, the only physical alignment involves translation of the PPLN crystal to the corresponding QPM channel, which can easily be automated [14]. Thus the setup of Fig. 1 is extremely flexible. In addition, by employing the OFAs shown in this figure, one is able to achieve mid-IR powers as high as 1 mW, far in excess of that required for compensating the insertion loss of most multi-pass absorption cells. Depending on the effective pathlength and resulting transmission loss through such multi-pass cells, the generated power can be adjusted to be an optimal balance between the noise level of the detectors and optical background introduced by mirror scattering effects. In many cases, particularly in multi-pass absorption measurements, excessive mid-IR power of more than a couple of hundred μW typically does not improve the signal-to-noise but only increases background scatter. This ability to decouple the operating wavelength from the laser power is one of many advantages offered by DFG laser sources. Power levels of

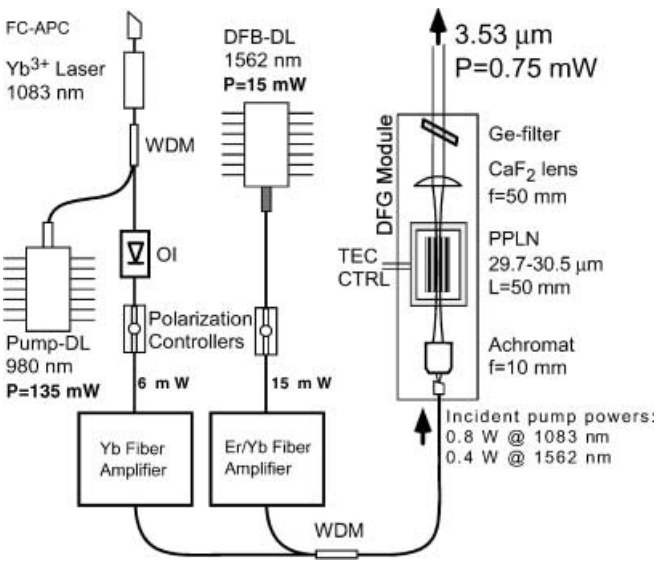

FIGURE 1 Robust near 'turn-key' all-fiber-coupled mW level tunable mid-IR source based on difference frequency generation operating at room temperature

$\sim 25\,\mu$W onto the detector (at fractional absorbances of 10^{-6}) is more than sufficient to operate above the inherent detector noise level. In the present study we employ a 100-m pathlength astigmatic Herriott cell with 182 passes and a nominal mirror reflectivity of 99.0%, which requires a mid-IR laser power of $\sim 156\,\mu$W. However, optical powers up to $417\,\mu$W would be required if the mirror reflectivity degrades to 98.5% (cell transmission $\sim 6.3\%$), as was observed with the present cell after two extended airborne field campaigns over very polluted regions. It is important to note that with these degraded mirrors the cell transmission was worse ($\sim 2.5\%$) for both a lead-salt diode laser operating in the same wavelength region ($2800\,\mathrm{cm}^{-1}$) as well as a quantum cascade laser in the $1260\,\mathrm{cm}^{-1}$ region. The significantly better beam quality of the DFG laser source is responsible for this improved multipass cell transmission. Subsequent cleaning of the mirrors from accumulated airborne particles and micro-fibers with an Orvus© solution regained an effective DFG transmission of 20%. Typical cell transmission with the lead-salt diode with clean mirrors is $\sim 12-16\%$. Disselkamp et al. [16] further discuss the relationship between laser beam profile and instrument performance for quantum cascade lasers with regards to susceptibility to optical feedback and the high divergence of the output beam.

3 Performance characteristics of the seed lasers and DFG

In the following section the spectroscopic performance of the DFG ('idler') seed laser sources commonly referred to as 'pump' and 'signal' are discussed.

4 'Pump' laser: diode laser-pumped fiber laser

A relatively new and extremely narrow linewidth fiber laser source [17] is employed as the pump source, operating at 1083 nm with an output power of 6 mW. The operating configuration of the fiber laser is depicted in Fig. 1. A fiber Bragg grating-stabilized high-power ($P_{\mathrm{out,\,fiber}} = 135\,\mathrm{mW}$) pump laser at 980 nm is fusion-spliced to a WDM and coupled to a short Yb-doped fiber with a superimposed distributed feedback (DFB) grating. The DFB grating is configured such that the laser output is opposite to the direction of the 980 nm pump laser radiation (downward in Fig. 1) and is coupled out via the second leg of the WDM. The non-absorbed 980 nm pump radiation is dumped through an angle polished connector (FC-APC) at the top of the fiber laser also shown in Fig. 1. Past the WDM, two optical isolators in series provide a combined optical isolation of -70 dB. In such a configuration, the fiber laser exhibits very low noise operation (side mode suppression ratio = 65 dB) and a linewidth of less than 100 kHz, as measured with self-heterodyne measurements. Such very narrow 'free-running' linewidths of fiber lasers are usually only obtained with semiconductor lasers with external feedback elements or active frequency locking [18]. We investigated the fiber laser's operating characteristic wavelength tuning induced by changes in ambient temperature and changes in the 980 nm pump diode power and temperature. The tuning rate of the fiber laser was measured to be $-0.18\,\mathrm{cm}^{-1}\mathrm{K}^{-1}$ and is primarily determined by the aluminum substrate on which the active fiber is mounted. The laser can be operated from $-40\,^{\circ}$C to $60\,^{\circ}$C and hence provides an ample wavelength tuning range ($+/-9\,\mathrm{cm}^{-1}$) around its designed operating wavelength ($+/-0.1$ nm). On the other hand, this requires active temperature control of the fiber laser mount to avoid frequency drift in the mid-IR. Hence, the fiber laser was mounted on a Peltier element controlled by a precision temperature controller ($0.001\,\mathrm{K\,h}^{-1}$ stability). The measured response of the fiber laser due to changes of the pump diode laser power and operating temperature were negligible at $0.0003\,\mathrm{cm}^{-1}\,\mathrm{mA}^{-1}$ and $0.001\,\mathrm{cm}^{-1}\mathrm{K}^{-1}$, respectively. Given that the precision of the current (5 μA noise ripple) and temperature drivers ($0.001\,\mathrm{K\,h}^{-1}$) are similar to those for the DFB diode laser (signal laser, see Sect. 2), the pump diode laser has no noticeable effect on the frequency stability of the fiber laser output.

5 'Signal' laser: fiber pigtailed distributed feedback (DFB) diode laser

A fiber pigtailed DFB diode laser was employed as the 'signal' wavelength, similar to the previous designs of fiber-based DFG laser sources [9, 15]. Here, a more powerful (15 mW) and narrower linewidth telecommunication grade laser is mounted in a hermetically sealed package (14-pin butterfly) and fitted with a Peltier element for active temperature control and a -55 dB optical isolator. This diode laser exhibits very low noise (SMR = 46 dB) and narrow linewidths of ≤ 1 MHz. The effective tuning rates for changes of temperature ($-0.39\,\mathrm{cm}^{-1}\mathrm{K}^{-1}$) and current ($22\times10^{-3}\,\mathrm{cm}^{-1}\mathrm{mA}^{-1}$) were measured using a high-resolution wavemeter (0.001 nm). This provides coarse wavelength tuning of $6.5\,\mathrm{cm}^{-1}$ and rapid fine-tuning of more than $1\,\mathrm{cm}^{-1}$, and thus permits scanning of single, and in some cases, multiple absorption lines ranging from Doppler-limited to pressure-broadened lineshapes at atmospheric pressures. In a DFG source using the described seed laser sources, temperature effects exclusively determine the drift. However, in the case of DFG, the frequency drifts of the seed laser wavelengths are effectively canceled. Considering the measured temperature tuning coefficients for the pump and signal lasers, a net frequency tuning of $-0.21\,\mathrm{cm}^{-1}\mathrm{K}^{-1}$ is obtained, resulting in effective frequency drifts that are equal or less than the DFG linewidth during a typical acquisition time of 60 s. This can further be improved by mounting the fiber laser on a substrate that exactly matches the tuning rate of the 'signal' laser and thus perfectly cancels the thermally induced laser frequency drifts. This approach takes into account both differential temperature-dependent tuning rates inherent to the laser and temperature dependence of the employed laser and temperature controllers.

For highly sensitive absorption spectroscopy, it is also important that the scanning laser exhibits no 2nd order wavelength tuning (i.e. the rate of change in the tuning is linear). Although this aspect is not the limiting factor in our present spectroscopic measurements, it may become important in order to detect absorptions at the 1×10^{-7} level. For example, small changes in background structure over a 2nd order non-linear scan portion can translate into significantly larger background changes than would otherwise be the case. This could be exacerbated by any wavelength jitter and drift. In addition, such wavelength jitter when coupled with a 2nd

order non-linear scan could in turn add 'weighted' noise when one attempts to fit a sample spectrum to a previously acquired calibration spectrum. By applying a range of different wavelength scanning current ramp functions (saw-tooth, soft-saw-tooth and triangular ramps) to the signal laser, we measured the respective 2nd order tuning non-linearity using a solid Ge etalon ($L = 7.62$ cm; FSR $= 0.016\,\mathrm{cm}^{-1}$). In general, all current waveforms applied to the signal laser resulted in a 1st order non-linearity (linear increase in $\mathrm{cm}^{-1}\mathrm{mA}^{-1}$ over the scan ramp). However, in the case of the saw-tooth function, the tuning exhibits a 2nd order non-linearity (exponential function), which is present in the first 30–50% of the entire scan. By implementing a tanh function on the saw-tooth recovery (soft-saw-tooth), the 2nd order non-linearity is reduced, but not eliminated. In addition, as much as 20% of the total scan width is needed in order to reduce this 2nd order non-linearity. Using a triangular waveform, no 2nd order non-linearity was observed. The signal laser exhibited a tuning rate of $\sim 1 \times 10^{-3}\,\mathrm{cm}^{-1}\mathrm{channel}^{-1}$ and a 1st order non-linearity of $8 \times 10^{-6}\,\mathrm{cm}^{-1}\mathrm{channel}^{-1}$ (500 channel/scan). This 1st order non-linearity is easy to account for in normalizing the wavelength scan, and if fitted out by a linear post facto subtraction, provides a total deviation of as little as 1×10^{-8} ($4 \times 10^{-9}\,\mathrm{cm}^{-1}$ over a total scan rate of $0.4\,\mathrm{cm}^{-1}$) [15].

6 Optical fiber amplifiers (OFA)

Two high-power rare-earth-doped OFAs providing amplification via Yb gain @ 1083 nm (> 30 dB m; 3 dB BW 25 nm) and Er/Yb gain @ 1550 nm (> 27 dB m; 3 dB BW 30 nm) are employed [19]. Common features for both OFAs are high optical input isolation and optical pumping by multimode-coupled broad-stripe diode lasers at ~ 975 nm. Due to higher insertion loss optical fiber isolators at ~ 1 μm wavelengths, the Yb-OFA higher output power is operated with no optical output isolation. Er/Yb-OFA offers low loss input and output optical isolation (35 dB) due to material advancements, even at higher power levels. Care is taken to avoid back reflections into the Yb-OFA by very low return losses through optical fiber fusion splices, WDM and final termination by an angle-polished fiber connector providing −67 dB return loss. Both amplifiers were tested for long-term power stability. If seeded by the aforementioned laser sources, the Yb-OFA and Er/Yb OFA provide a measured power stability (std. dev.) of $0.27\%\,\mathrm{h}^{-1}$ and $0.17\%\,\mathrm{h}^{-1}$, respectively.

7 Difference frequency generation (DFG)

Using the above-described pump and signal laser sources, tunable ($\sim 16\,\mathrm{cm}^{-1}$) DFG radiation of 0.75 mW was measured (accounting for insertion losses of the Ge filter and CaF_2 collimation lens of 4% and 5.8%, respectively), with incident power levels of 0.43 W and 0.87 W at 1563 nm and 1083 nm, respectively. This corresponds to a normalized conversion efficiency of $0.4\,\mathrm{mW\,W}^{-2}\,\mathrm{cm}^{-1}$. The present current driver used for the Yb pump diode laser is limited to supply 75% of the rated operating currents. Thus by using a higher rated power supply, DFG powers of 1 mW have been achieved with the current system. The use of highly saturated two-stage optical fiber amplifiers provides superior stable power operation, free of any spectral intermittences caused by backscattered radiation and non-linear optical fiber effects such as stimulated Brillouin scattering [20].

The spatial beam profile of the DFG radiation was measured at different distances from the imaging CaF_2 lens. For this purpose we used an automated beam profiler, (Dataray Beamscope-P5; scanning 100 μm pinhole $y = 35\,\mathrm{mm} \times x = 45\,\mathrm{mm}$) equipped with a sensitive room temperature mid-IR II-VI detector. Figure 2 shows the DFG beam at a distance of 37.5 cm from the PPLN output facet. The cross-section of the measured beam is uniform, circular, and fits to a Gaussian intensity profile to better than 95%. From this weakly focusing position, the CaF_2 lens was then incrementally translated towards the PPLN crystal to obtain optimal imaging and collimation of the DFG radiation at a distance of ~ 50 cm from the PPLN crystal output facet. At this distance, the beam was measured over the length of the mirror separation (55 cm) of the astigmatic Herriott cell used in this work. Figure 3 shows the beam diameter measured at $1/e^2$ and the intensity cross-section for various corresponding locations of the Herriott cell. Again, the beam shows a uniform and Gaussian spatial beam profile and indicates an effective collimation with an $f/\#$ of 130. The ordinate axis of Fig. 3 is also scaled for the input mirror coupling hole diameter (10 mm in this case), further indicating that a well-defined beam with a high $f/\#$ is far less susceptible to clipping, thereby potentially causing additional background noise. The < 2.5 mm beam diameter can be used with even smaller coupling holes employed in Herriott cells with longer pathlengths. To our knowledge, this is the first published report of the beam profile from a DFG laser source obtained at different corresponding positions of a Herriott cell. In addition, it is important to emphasize that the measurements shown in Fig. 3 were obtained using only one optical element after the PPLN stage and this element was positioned ~ 5 cm from the stage. This results in a very simple

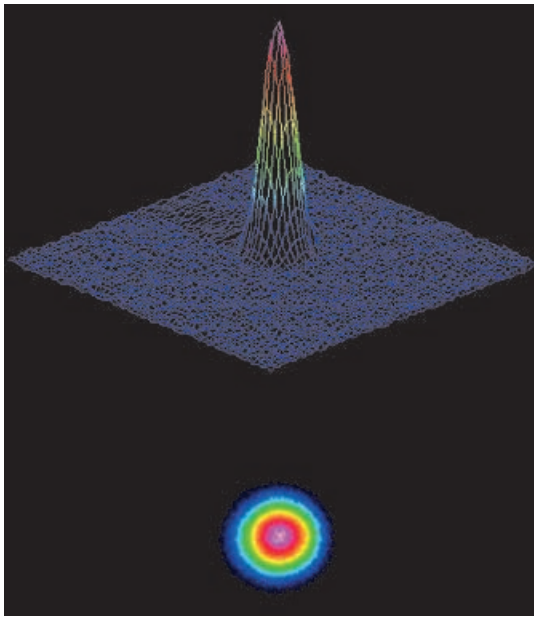

FIGURE 2 DFG mid-IR spatial beam quality. The weakly focused beam was measured 37.5 cm past the PPLN crystal output facet. Measured beam widths: $x = 0.8$ mm; $y = 0.8$ mm; Gaussian fit = 95%. The Gaussian fit is defined here as absolute sum of profile differences divided by the total area

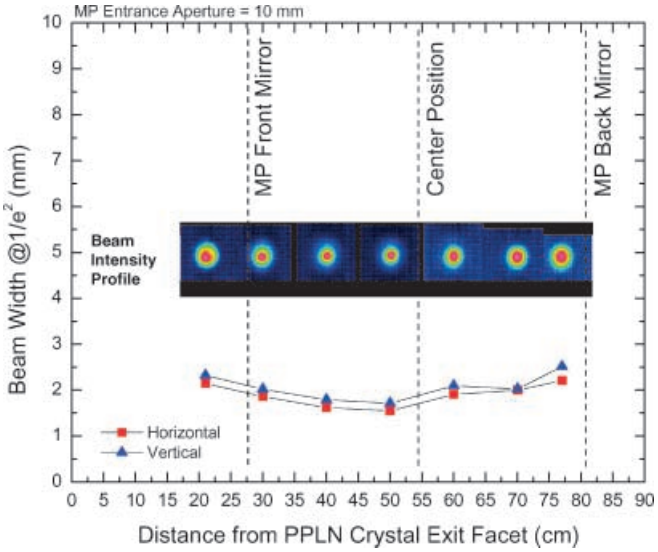

FIGURE 3 Mid-IR beam propagation of the collimated DFG beam (f/#130) collected by a $f = 50$ mm plano-convex CaF_2 lens. Also shown are the physical overlap of the mid-IR beam with the multi-pass absorption cell in terms of mirror separation and input coupling hole diameter (10 mm). MP, multi-pass absorption cell

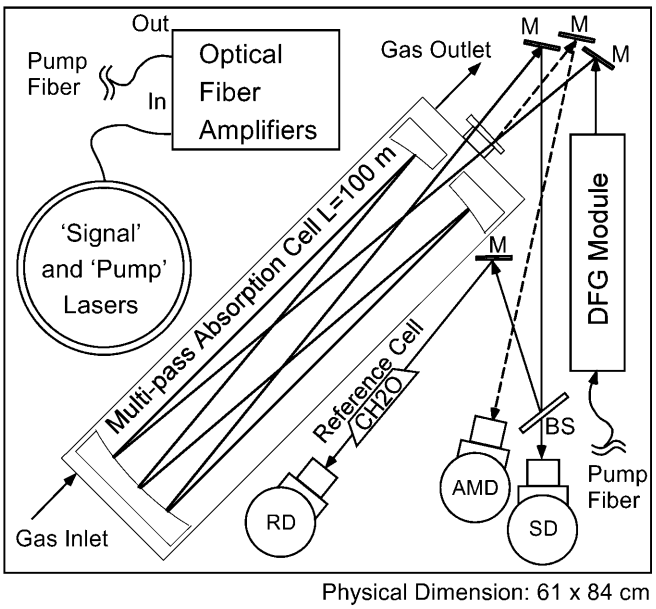

FIGURE 4 Schematic of the airborne trace gas sensor platform. M, mirror; BS, beam splitter; RD, reference detector; AMD, amplitude modulation detector; SD, sample detector

and compact transfer optical system, which ultimately can be mounted directly to the Herriott cell for very high beam pointing stability. By contrast, the corresponding transfer optics employed with lead-salt and quantum cascade lasers mounted in cryogenically cooled dewars require multiple optical elements that must be mounted at certain fixed positions for efficient spatial mode-matching through the Herriott cell. Thus, in a typical lead-salt or quantum cascade laser setup, the laser beam traverses at least 1 m pathlength before entering the Herriott cell. This long optical lever arm is less stable than a DFG system. The compact DFG transfer optics, moreover, readily allows for dust-free operation in a pressure-controlled environment, both of which are important for aircraft operation.

8 Spectroscopic absorption measurements of formaldehyde (CH_2O)

To validate the performance of the DFG source described in the previous section, a series of spectroscopic measurements were carried out in our laboratory using CH_2O as the test gas. Figure 4 shows the compact arrangement of the DFG source, astigmatic Herriott-type multi-pass absorption cell [21] and detectors. Most of the essential equipment and procedures including gas flow and calibration, sweep integration second harmonic detection, data acquisition hardware and software code, and modulation spectroscopy electronics is based on the lead-salt diode laser system developed by Fried et al. [7, 22]. It is important to note that the data processing algorithms, gas flow and calibration systems have all been extensively studied and optimized to ensure accurate and absolute absorption measurements, a requisite for meaningful performance evaluations [23].

The optical setup shown in Fig. 4 and the acquisition sequence detailed in Table 1 were used to acquire the results discussed here. In our spectroscopic measurements we employed the technique of sweep integration second harmonic detection coupled with rapid background acquisition.

Time Start (Sec)	Acquisition Type	Acquisition Time (Sec)	Acquired Variable	
0	Bkg_1	10	$(SD\text{-}AMD)_1$	
10	Flushing + Overhead	10		
20	Amb_1	5	$(SD\text{-}AMD)_1$	
25	Amb_2	5	$(SD\text{-}AMD)_2$	
30	Amb_3	5	$(SD\text{-}AMD)_3$	AvgBkg
35	Amb_4	5	$(SD\text{-}AMD)_4$	
40	Flushing + Overhead	10		
50	Bkg_2	10	$(SD\text{-}AMD)_2$	

TABLE 1 Data acquisition sequence for Figs. 5–7. The acquisition types Bkg_1 and Bkg_2 are the 1st and 2nd zero air background acquisitions; Flushing + Overhead is the delay period between acquisitions to allow for 5 cell/inlet e-fold exchanges plus 2 s data processing overhead; Amb_1 to Amb_4 are the successive ambient acquisitions, which in this case are zero air additions; SD and AMD are the sample detector and background detector signals as defined in Fig. 4; and the average background AvgBkg is obtained from the average of $(SD\text{-}AMD)_1$ and $(SD\text{-}AMD)_2$

For this purpose a scan ramp/modulation waveform was applied to the signal laser. A saw-tooth current ramp, employing a soft tanh roll-off at 50 Hz and quasi square-wave at 50 kHz with a modulation depth (modulation halfwidth/line halfwidth) of 2 was generated using a computer-controlled DSP board. The mid-IR radiation was detected at 100 kHz using lock-in amplifiers. A detailed description of these approaches as well as the details of the data processing algorithms and calibration procedures are reported by Fried et al. [22] and Lancaster et al. [9] These same approaches are used here only with the addition of the amplitude modulation detector (AMD) shown in Fig. 4 (to be discussed). The following acquisition parameters are employed for the results shown here: cell pressure = 5.3 kPa; cell temperature = 296 K; pathlength = 100 m; cell flow rate = 9.1 standard liter min^{-1} (standard conditions of 101.3 kPa, 273 K).

Zero air backgrounds are acquired by replacing the ambient sample flowing through the inlet and Herriott cell with

an excess flow of zero air, which is generated using a heated Pd/Al_2O_3 scrubber unit. This unit effectively scrubs CH_2O without significantly affecting the ambient water vapor in the sample stream. Each ambient and calibration spectrum has an associated pair of backgrounds acquired before and after. As discussed by Fried et al. [22], subtraction of the averaged background spectrum from the intervening sample or calibration spectrum very effectively eliminates optical fringe noise caused by scattering from various optical elements. However, this approach may be less effective in eliminating the very large optical structures caused by residual amplitude modulation (RAM) from the 1.56 μm 'signal' laser and from optical fringes caused by refractive components in the 'signal' arm (fiber optic link from the signal laser output facet to the DFG module, which is terminated by an angled optical fiber connector). Since the 'signal' arm is scanned and modulated, the above two noise sources, which will be frequency down-converted into the mid-IR spectral region, will also be transmitted effectively through the entire signal detection chain.

As the magnitude of the RAM signal may be large (10^{-4}), real time acquisition of the RAM before the multi-pass absorption cell using the AMD shown in Fig. 4 concurrent with simultaneous sample detector (SD) measurement becomes very important. Figure 5 displays such large 'fringe-like' features detected by the SD and AMD. The optical structure in Fig. 5a and b is similar in shape, as would be expected since zero air is flowing through the multi-pass absorption cell for these scans. The magnitude of these signals in terms of absorbance and/or equivalent CH_2O concentration can be obtained by referring to Fig. 6, where a 20 s calibration spectrum is acquired by the addition of a 13.6 ppbv CH_2O standard (line center absorbance $= 4.5 \times 10^{-4}$). A comparison of the peak-to-peak signal from the calibration profile of Fig. 6 with that from the sample detector in Fig. 5 between channels 70 and 150 (the scan window where the CH_2O absorption occurs) indicates an equivalent peak absorbance $\sim 8 \times 10^{-4}$ for the RAM feature. At the start of the scan (channel 0 to ~ 70) the amplitude is even larger ($\sim 1.3 \times 10^{-3}$), and as previously discussed, the RAM here is most likely accentuated by the 2nd order non-linearity in the tuning current from our sawtooth sweep ramp. Clearly these large background features make it very challenging to detect CH_2O absorbances in the 10^{-6} range, and strategies must be implemented for eliminating these features. One can reduce these 'fringe-like' features significantly by employing the AMD detector, as will be discussed below.

Table 1 shows the acquisition sequence employed. First a 10 s background spectrum is acquired by adding zero air into the multi-pass absorption cell, and the resultant large optical features from both the SD and AMD are recorded. Figure 5 (Bkg_1 traces at time $T = 0$ seconds) shows these features for both detectors. After an appropriate flushing period, to allow for ~ 5 cell/inlet line e-folding periods as well as processing overhead, a succession of four 5 s 'ambient samples' are acquired. In this particular case, the 'ambient samples' are actually zero air. This is followed by another flushing period and ultimately the acquisition of a second zero air background ($Bkg_2 \sim 50$ seconds after the start of the first zero air background). As indicated in Table 1, in each case the AMD signal is subtracted point-by-point from the sample detector signal (SD–AMD) averaged over the 5 s ambient or 10 s background phases. We now acquire and subtract the background profile on every 20 ms scan, but this only minimally improves the results from those above. As can be seen

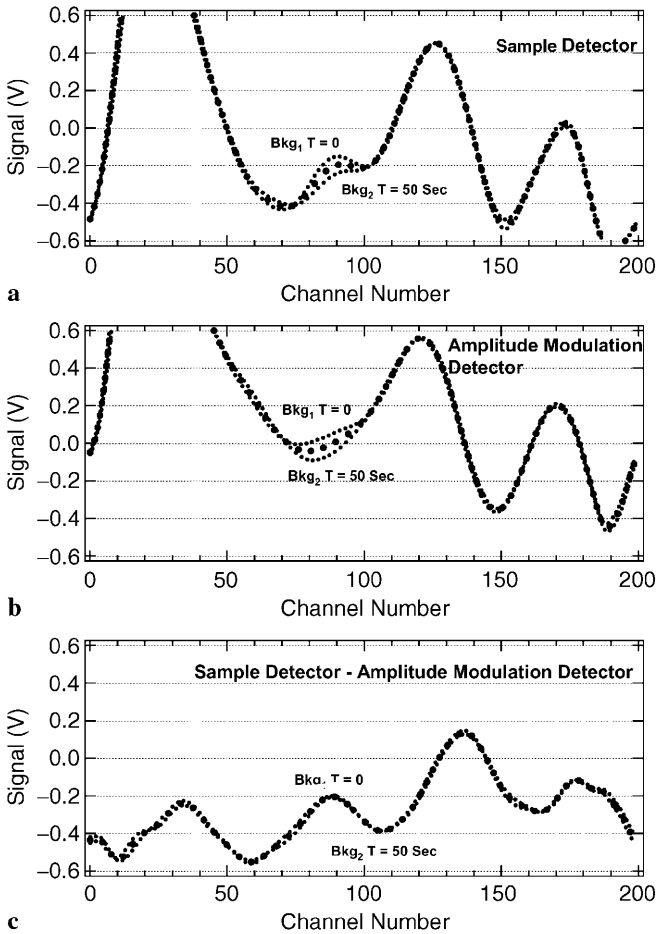

FIGURE 5 Background fringe-like RAM features captured by **a** the sample detector; and **b** the amplitude modulation detector along with **c** the point-by-point difference. See text for detailed explanation

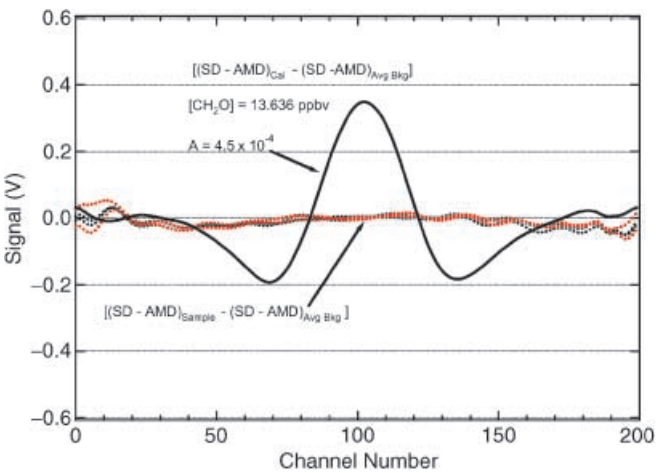

FIGURE 6 Four replicate 'ambient' acquisitions employing the data acquisition sequence of Table 1 and the recovered absorption signal (2831.6417 cm^{-1}) from a 13.6 ppbv gas standard

in Fig. 5a and b, the background structure smoothly evolves from the start of the first through the second zero air acquisitions 50 s apart. Thus the average background for both the SD and AMD are represented by the average feature (center-dotted traces). Figure 5c shows the result of subtracting the AMD from the SD for the first, second and average zero air background acquisitions. As indicated in Table 1, we ultimately use the average background (AvgBkg) in our data processing, i.e. the average of $(\text{SD-AMD})_1$ and $(\text{SD-AMD})_2$ (the center-dotted trace of Fig. 5c). This procedure reduces the large optical noise by approximately $1/2$ over the CH_2O absorption region and by a significantly greater factor at the start of the scan, as shown in Fig. 5c. On some occasions the RAM removal by the AMD is near perfect (almost flat profiles). However, Fig. 5c is more the norm, and this is caused by small residual differences in the two detection arms (hereafter referred to as residual RAM), including phase differences, dc differences and shape differences, as can be seen in Fig. 5a and b. Future efforts will focus on better matching of these two channels.

Although the residual RAM of Fig. 5c is still relatively large, it is constant over the two background acquisitions 50 s apart. This makes it possible to use the background spectra to remove the residual RAM during the inserted 'ambient samples'. This is accomplished by using the AvgBkg to subtract from each of the 'ambient samples', where the SD-AMD is derived. Thus, the residual RAM captured by the AvgBkg is also captured by the 'ambient samples'. The effectiveness of this approach is shown in Fig. 6, where the AvgBkg has been removed from the four 'ambient samples'. Thus the frequent zero air background acquisitions before and after the 'ambient samples' are means of correcting for the residual RAM. Because of the magnitude variability of the original RAM signal, applying the AMD correction more frequently is more effective than simple background subtraction.

Fitting the four 'ambient samples' to the calibration spectrum of Fig. 6, where the calibration is treated exactly analogous to the 'ambient samples' of Table 1 (i.e. $(\text{SD-AMD})_{\text{cal}} - \text{AvgBkg}_{\text{cal}}$) yields an average retrieved fit concentration of 90 pptv$\pm$86 pptv. While perfect removal of the background features would produce a retrieved value of 0, this procedure results in a factor of 300 improvement in measurement performance over the structure of Fig. 5a (86 pptv 1σ precision corresponds to an absorbance of $\sim 2.9 \times 10^{-6}$ for a 50 s net measurement period, 20 s of which were used in acquiring the 'ambient sample'). However, it is more meaningful to determine if repeated sampling sequences of Table 1 result in the same performance. The results of this procedure are shown in Fig. 7. Here, the resulting 20 s ambient averages are plotted along with the standard deviation of each determination ($n = 4$). As can be seen by the composite average (76 pptv) and standard deviation ($\pm$159 pptv) of ten such determinations, the longer-term effectiveness of our RAM removal approach degrades slightly from the performance of Fig. 6. Nevertheless, the 159 pptv precision corresponds to a 1σ absorbance of $\sim 5 \times 10^{-6}$, which is remarkable considering the size of the initial RAM signals of Fig. 5a and b. For comparison, employing background subtraction without using the AMD results in a composite average and

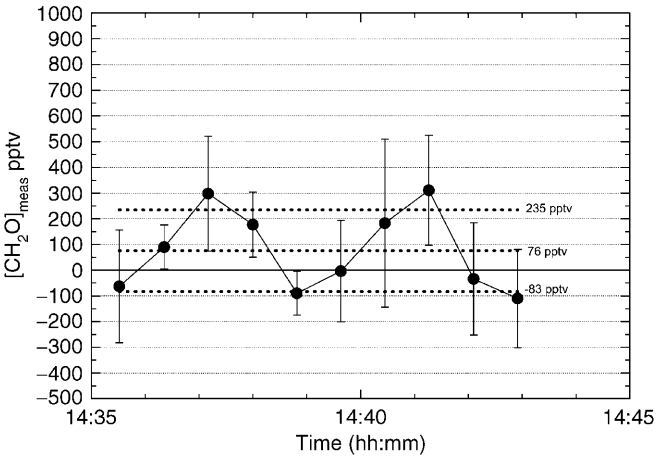

FIGURE 7 The results of repeated sampling sequences in Table 1. Each point represents the retrieved results and the $\pm 1\sigma$ upon acquiring four times 5 s 'ambient' measurements. The 'ambient' samples shown here and in Fig. 6 and 8 were acquired using zero air. The 2nd retrieved point shown here was determined by fitting the four spectra of Fig. 6 to the calibration spectrum of that figure

standard deviation of 93 ± 295 pptv, around a factor of 2 worse.

The CH_2O results of the present study can be compared directly to those of Lancaster et al. [9] and those of Fried et al. [7] using a lead-salt diode laser during the TOPSE [6] 2000 campaign. All three studies employed the same fundamental aircraft detection system (multipass absorption cell, inlet etc.), calibration, data analysis and fitting routines to detect CH_2O. The results of the present study based on RAM removal are about a factor of 2 better than those of Lancaster et al. [9] employing the same 20 s 'ambient' averaging time used here. Assuming a $(T)^{1/2}$ time dependence to extrapolate the present results to 1 min to match those employed by Fried et al. [9], the present precision of 92 pptv is only a factor of 2 higher than those typically obtained using a lead-salt laser (1σ precision of 40 pptv for 1 min of averaging).

Figure 8 shows the validity of the $(T)^{1/2}$ time dependence for another measurement set employing the RAM reduction technique. In this case we carried out the residual RAM correction every second: i.e. every 1 s 'ambient sample' was followed by 1 s background acquisitions with a delay time of 3–4 s in between due to data processing overhead. Although this approach is less efficient than the 20 s measurements above in terms of 'ambient' acquisition duty cycle (25 % here), these measurements indicate what ultimately is possible with the RAM reduction approach employing frequent residual RAM correction between the two detection chains. The original 1 s time series data and resultant 60 s block averages are displayed in the inset. The main figure shows how the measurement standard deviation improves with averaging time, and the dashed line gives the resultant fit of this improvement with time. Figure 8 indicates a 1σ measurement precision of 74 pptv for repeated ($N = 10$) 1 min averages. This slight improvement from the extrapolated results above (92 pptv) probably arises because of the more frequent residual RAM correction and the fact that a less perturbing triangular scan waveform was employed.

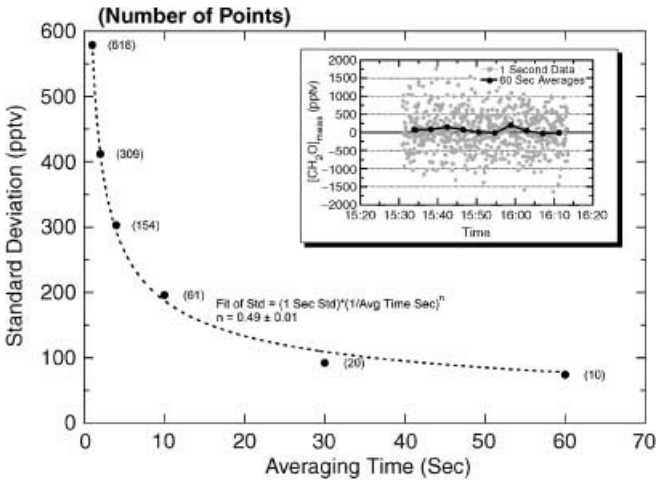

FIGURE 8 1 s 'ambient' results obtained when zero air backgrounds before and after were acquired every second with 0 delay. The $T^{1/2}$ improvement with averaging time results in a 1σ detection limit of 74 pptv for 1 min of averaging

9 Discussion and conclusions

The DFG-based laser source described here exhibits a number of improvements over previous designs [9], in terms of reliable and stable operation with respect to power (mW), narrow linewidth (sub-MHz) and spatial beam profile (near-Gaussian). This near 'turn-key' DFG-based mid-IR source operates reliably at room temperature with a factor of 2 improvement in detection limit from the prototype study [9]. For 1 min acquisition times, minimal detectable CH_2O concentrations of 74 to 92 pptv are possible. RAM has been experimentally verified as the dominating noise factor in the present system, which currently prevents even higher absorption sensitivity. Although RAM is captured employing a second detector, subtle residual differences in the two detector chains requires frequent correction at the expense of a reduced measurement duty cycle. Inherent small drifts present in the lock-in amplifiers used for demodulating the 2-f signal from the AMD and SD are responsible for these residual differences.

An alternative and more promising approach to reduce the large RAM is presently being implemented using a novel form of an AM-flattening fiber servo module. As demonstrated by Wong and Hall [24], using a slightly different method to achieve such AM-flattening, this approach should permit the real-time elimination of RAM and any other spurious sources of dynamically drifting optical fringes prior to the input window of a multi-pass absorption gas cell. This approach, furthermore, is not susceptible to drifts between the AMD and SD chains, as in the present study. Alternatively, such a servo amplitude modulator can also be simultaneously implemented in a PPLN-based conversion crystal [25], however, at the expense of a reduced conversion efficiency and in some cases generation of frequency sidebands. For future airborne missions, the DFG module will be mechanically integrated with a longer pathlength multi-pass cell ($L = 210$ m) into a single solid unit. In addition to a factor of 2 larger absorption, this should further reduce the perturbation from adverse physical effects on the optical system during airborne operation. Implementation of an amplitude servo, longer pathlength multi-pass absorption cell and mechanical integration with the DFG module may permit pathlength-normalized field absorption sensitivities of equal or better than 1 to 5×10^{-11} cm^{-1}.

ACKNOWLEDGEMENTS The National Center for Atmospheric Research is sponsored by the National Science Foundation. This work was also funded in part by the National Oceanic and Atmospheric Administration under Grant No. GC00-015. The authors would like to thank Dr. James F. Kelly (Pacific Northwest National Laboratories, WA) for helpful discussions and Dr. William Potter (University of Tulsa, OK) for the generous loan of a mid-IR beam profiler.

REFERENCES

1 P. Werle: Spectrochim. Acta A **54**, 197 (1998)
2 F.K. Tittel, D. Richter, A. Fried: 'Mid-Infrared Laser Applications in Spectroscopy'. In: *Solid-State Mid-Infrared Laser Sources*, ed. by I.T. Sorokina, K.L. Vodopyanov, (Springer Verlag, in press)
3 I.T. Sorokina, E. Sorokin, A. Di Lieto, M. Tonelli, R.H. Page, K.I. Schaffers: J. Opt. Soc. Am. B **18**, 926 (2001)
4 L.R. Narasimhan, W. Goodman, C.K.N. Patel: Proc. Natl. Acad. Sci. **98**, 4617 (2001)
5 M.W. Sigrist: 'Air Monitoring by Spectroscopic Techniques'. In: Chemical Analysis, Vol. 127 (John Wiley, New York 1994)
6 'TOPSE': http: //topse.acd.ucar.edu/
7 A. Fried, Y. Wang, C. Cantrell, B. Wert, J. Walega, B. Ridley, E. Atlas, R. Shetter, B. Lefer, M.T. Coffey, J. Hannigan, D. Blake, N. Blake, S. Meinardi, B. Talbot, J. Dibb, E. Scheuer, O. Wingenter, J. Snow, B. Heikes, D. Ehhalt: J. Geophys. Res., Special TOPSE Issue (2002)
8 Note, *Low RAM is typically achieved with lasers that have very small laser linewidth enhancement factors (α factor).* Pb-*salt diode laser have very low α factors, about* 2–3 *times lower than near-IR diode lasers and about 10 times lower than quantum cascade laser sources*. Personal Communications with Dr. James F. Kelly, PNNL
9 D.G. Lancaster, A. Fried, B. Wert, B. Henry, F.K. Tittel: Appl. Opt. **39**, 4436 (2000)
10 K.P. Petrov, S. Waltman, U. Simon, R.F. Curl, F.K. Tittel, E.J. Dlugokencky: Appl. Phys. B **61**, 553 (1995)
11 K.P. Petrov, A.P. Roth, T.L. Patterson, T.P.S. Thoms, L. Huang, A.T. Ryan, D.J. Bamford: Appl. Phys. B **70**, 777 (2000)
12 D. Richter, D.G. Lancaster, R.F. Curl, W. Neu, F.K. Tittel: Appl. Phys. B **67**, 347 (1998)
13 M. Seiter, M.W. Sigrist: Appl. Opt. **38**, 4691 (1999)
14 D. Richter, D.G. Lancaster, F.K. Tittel: Appl. Opt. **39**, 4444 (2000)
15 D. Richter, A. Fried, G.S. Tyndall, E. Oteiza, M. Erdelyi, F.K. Tittel: *Advanced Solid State Lasers, Technical Digest* WA3 (2002)
16 R.S. Disselkamp, J.F. Kelly, R.L. Sams, G.A. Anderson: Appl. Phys. B, **75**, 359 (2002), 10.1007/s00340-002-0944-2
17 N. Matsuoka, S. Yamaguchi, K. Nanri, T. Fujioka, D. Richter, F.K. Tittel: Jpn. J. Appl. Phys. (1) **40**, 625 (2001)
18 R.W. Fox, L. Hollberg, A.S. Zibrov: 'Semiconductor Diode Lasers'. In: *Atomic, Molecular, and Optical Physics: Electromagnetic Radiation*, ed. by F.B. Dunning, R.G. Hulet (Academic Press 1997)
19 P.C. Becker, N.A. Olson, J.R. Simpson: 'Erbium-Doped Fiber Amplifiers, Fundamentals and Technology'. In: *Optics and Photonics*, ed. by P.L. Kelly, I. Kaminov, G. Agraval (Academic Press, San Diego 1999)
20 D.G. Lancaster, D. Richter, R.F. Curl, F.K. Tittel, I. Goldberg, J. Koplow: Opt. Lett. **24**, 1744 (1999)
21 J.B. McManus, P.L. Kebbabian, M.S. Zahniser: Appl. Opt. **34**, 3336 (1995)
22 A. Fried, B. Henry, B. Wert, S. Sewell, J.R. Drummond: Appl. Phys. B **67**, 317 (1998)
23 B.P. Wert, A. Fried, B. Henry, S. Cartier: J. Geophys. Res. 107(D13), 10.1029/2001JD001072 (2002)
24 N.C. Wong, J.L. Hall: J. Opt. Soc. Am. B **2**, 1527 (1985)
25 K.W. Wang, A.C. Chiang, T.C. Lin, B.C. Wong, Y.H. Chen, Y.C. Huang: Opt. Commun. **203**, 163 (2002)